OPEN ACCESS

University of BRISTOL

Peer reviewed version

License (if available):
CC BY-NC-ND

Link to published version (if available):
10.1016/j.apsusc.2019.04.053

Link to publication record in Explore Bristol Research
PDF-document

University of Bristol - Explore Bristol Research
General rights

High-performance photoluminescence-based oxygen sensing with Pr-modified ZnO nanofibers

Tingting Jiang[a,#], Baosheng Du[b,#], Hong Zhang[b], Dengfeng Yu[b], Lei Sun[a], Gongyuan Zhao[a], Chenhui Yang[a], Ye Sun[b,*], Miao Yu[a,*], and Michael N.R. Ashfold[c,*]

[a] *State Key Laboratory of Urban Water Resource and Environment, School of Chemical Engineering and Technology, Harbin Institute of Technology, Harbin 150001, China*

[b] *Condensed Matter Science and Technology Institute and Department of Physics, School of Science, Harbin Institute of Technology, Harbin 150080, China*

[c] *School of Chemistry, University of Bristol, Bristol BS8 1TS, U.K.*

Abstract

Praseodymium (Pr)-modified zinc oxide (ZnO) nanofibers have been fabricated using an electrospinning-calcination method. These Pr-modified ZnO nanofibers present porous morphologies containing numerous ZnO nanocrystallites with average sizes that are much smaller than those found in pure ZnO nanofibers formed by the same procedures. Most Pr is identified at the surface of / interface between the nanocrystallites. In addition to the morphological modifications, addition of Pr is also shown to enhance the crystalline quality of the ZnO. Consequently, the Pr-modified ZnO nanofibers have a higher UV emission efficiency and exhibit a much-enhanced UV emission-based O_2 sensing performance than the pure ZnO nanofibers. By way of illustration, the Pr-modified nanofibers show O_2 sensing responses of $R = 39\%$ at room temperature and $R = 71\%$ at 115 °C (*cf. R* = 19% and 52% with the pure ZnO nanofibers at these same operating temperatures). These results suggest that electrospun Pr-modified ZnO nanofibers hold real promise for high-performance optical gas sensing applications.

[#] Contributed equally to this work.

* Corresponding authors. E-mail address: miaoyu_che@hit.edu.cn (M. Yu), sunye@hit.edu.cn (Y. Sun), mike.ashfold@bristol.ac.uk (M.N.R. Ashfold)

1. Introduction

Optical gas sensors offer several distinctive advantages, which accounts for the intensity of current research in this area. In contrast to electrical sensors, optical sensors require no electrical contacts, can operate remotely and can be used in the presence of strong electromagnetic radiation or, for example, in aqueous solution [1−8]. Zinc oxide (ZnO) is widely regarded as one of the most promising optical gas sensing materials, on account of its acknowledged electrical sensing properties [9−13], high oxygen-adsorption capacity [14], excellent near-band edge UV emission properties [15,16] and the diversity of methods by which it can be produced at low cost and with different, but controllable, morphologies [17−22]. Various strategies, including controlling the morphology, crystal defects, doping, and surface modification have been reported to improve the UV-emission-based sensing performance of ZnO nanomaterials to target gases like O_2, H_2, CO, H_2S, NO_2, *etc.* [17−21,23−25]. However, there are at least two challenges that still need to be addressed in order to boost the practical application of ZnO-based optical gas sensors: (1) the UV emission efficiency and the sensing response both need to be improved further; and (2) a low cost and high yield growth technique needs to be adopted, since most ZnO nanomaterials with UV emission efficiencies sufficient for optical gas sensing applications reported to date were produced by high cost, low yield growth techniques like pulsed laser deposition [18−20] and chemical vapor deposition/vapor phase deposition [21,23−26]. Thus there remains a pressing need for a low cost, high yield production method for ZnO nanomaterials that display high UV emission intensities and high UV emission-based gas sensing responses.

The electrical gas sensing performance of ZnO and other oxides/hydroxides like SnO_2, Fe_2O_3 and $ZnSn(OH)_6$ can be notably enhanced by praseodymium (Pr) doping and modification [27−33]. Mechanistically, Pr species are assumed to facilitate oxygen chemisorption on the oxide surface and thereby enhance the gas sensing properties [28−33]. Addition of Pr has also been shown to influence the structure, morphology and, particularly, the light emission properties of ZnO [34−36]. These findings encouraged the present investigation of Pr-modified ZnO nanomaterials for potential optical gas sensor applications.

Electrospinning, followed by a calcination process, is one facile approach to producing oxide nanofibers with low cost and high yields [37−39]. The electrical gas sensing properties of electrospun oxide nanofibers have been widely explored [40−42], but their photoluminescence

2

(PL)-based gas sensing properties have not been reported hitherto. In this work, pure and Pr-modified ZnO nanofibers were fabricated using the same electrospinning-calcination production method, and their properties and performance compared. The pure ZnO nanofibers are found to consist of many compact nanocrystallites. The Pr-modified ZnO nanofibers, in contrast, present porous morphologies and are built up from many much smaller nanocrystallites. The latter nanofibers exhibit enhanced UV emission efficiencies, and more importantly, show a much-improved UV emission-based oxygen sensing performance (Fig. 1). Possible mechanisms for the enhanced sensing performance are discussed accordingly.
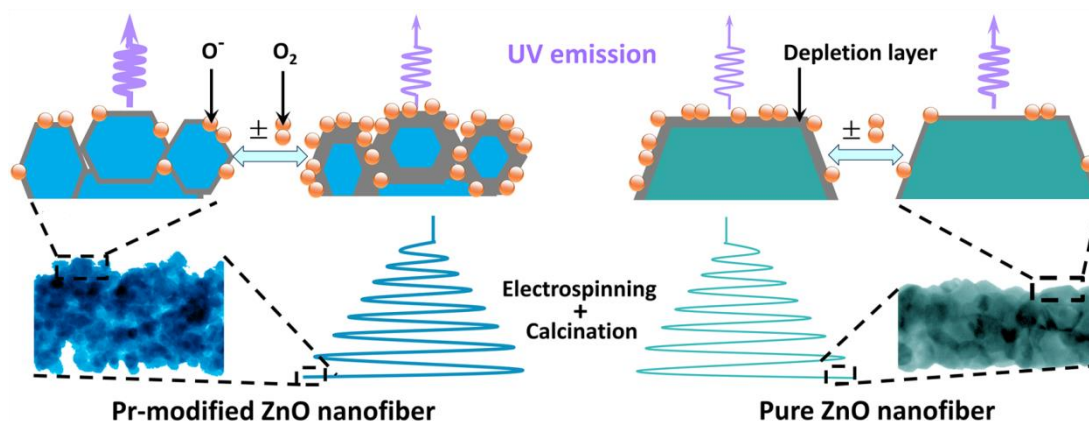

Fig. 1. Schematic illustration of the fabrication and oxygen gas sensing mechanism of the Pr-modified ZnO nanofibers.

2. Experimental

2.1. Synthesis of pure and Pr-modified ZnO nanofibers

Zinc nitrate hexahydrate $(Zn(NO_3)_2 \cdot 6H_2O)$ and N,N-dimethylformamide (DMF) were purchased from Sinopharm Chemical Reagent Co., Ltd; praseodymium nitrate hexahydrate $(Pr(NO_3)_3 \cdot 6H_2O)$ and poly(vinylpyrrolidone) (PVP, $M_w = 1,300,000$) were purchased from Aldrich. All chemicals were analytical grade and used as received without further purification. Pr-modified ZnO nanofibers were synthesized via an electrospinning method followed by a calcination process. In a typical procedure, solutions of zinc nitrate (594.8 mg $Zn(NO_3)_2 \cdot 6H_2O$) and praseodymium nitrate (8.7 mg $Pr(NO_3)_3 \cdot 6H_2O$) dissolved in DMF (4 mL) and of PVP (1.000 g) in ethanol (8 mL) were separately stirred for 6 h. The two solutions were mixed under stirring for 2 h and then loaded into

a glass syringe (needle diameter of 0.5 mm) connected to a high-voltage (15 kV) direct current power supply and composite nanofibers were electrospun onto the grounded collector electrode (an aluminum frame located at a distance of 20 cm), and then transferred to a standard thin mica microscope slide. Finally, a calcination process (at 500 °C in air for 5 h) was employed to selectively remove the organic constituents and achieve crystalline Pr-modified ZnO nanofibers (henceforth denoted as '*PZNF*'). For reference, pure ZnO nanofibers (denoted as '*ZNF*') were also synthesized using the same process but without the use of praseodymium nitrate hexahydrate.

2.2. Characterization

The products were characterized using scanning electron microscopy (SEM, FEI Quanta 200F, equipped with an energy dispersive X-ray spectrometer (EDS)), high-resolution transmission electron microscopy (HRTEM, FEI, Tecnai-G2-F30), X-ray diffraction (XRD, Rigaku D/MAX-2600/PC with Cu Kα radiation), X-ray photoelectron spectroscopy (XPS, ESCALAB, 250Xi), and spectrofluorometry (Horiba, Fluoromax-4, 325 nm excitation).

2.3. Optical gas sensing measurements

Temperature-dependent PL and UV emission-based gas sensing measurements were carried out using the spectrofluorometer together with a vacuum mini-chamber containing a heating system to allow variation of the sample temperature. The gas composition within the chamber was controlled using two mass flow controllers and one gas mixing chamber. The spectrofluorometer was used in 'kinetics' mode to derive real-time PL-based gas sensing data by monitoring the emission intensity at any user selected wavelength with a time resolution of 1 s. The O_2 sensing response of the samples at any temperature of interest is defined as $R = (I_0 - I_{100})/I_0$, where I_0 and I_{100} are the maximum values of the UV emission intensity measured in atmospheres of pure N_2 and pure O_2, respectively.

3. Results and Discussion

The morphologies of the as-prepared samples were first characterized by SEM and TEM. Figs. 2a and e present SEM images of the *ZNF* and *PZNF* samples, respectively. The *ZNF* sample is seen to consist of many uniform nanofibers with an average diameter, d ~180 nm. The Pr-modified ZnO nanofibers, in contrast, show a rough surface and larger average diameters, d ~330 nm. TEM

measurements further reveal that the pure ZnO nanofibers are comprised of many densely packed nanocrystallites with an average size of ~50 nm (Figs. 2b and c) whereas the *PZNF* samples present more porous structures containing many more, smaller crystallites with an average size of ~22 nm (Figs. 2f and g).
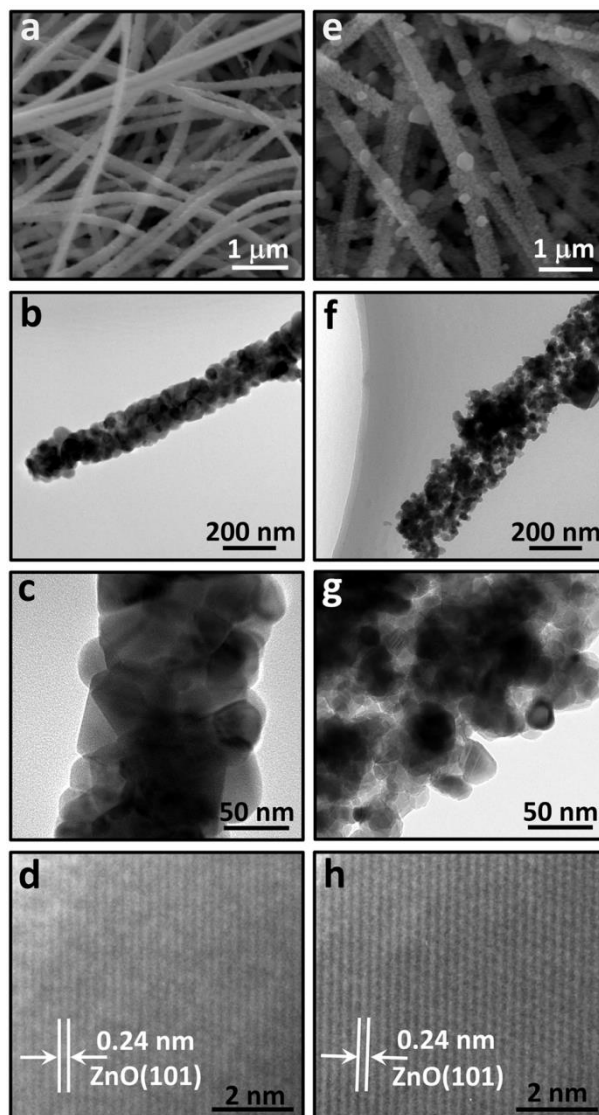

Fig. 2. SEM image, TEM images, and HRTEM image of (a–d) the *ZNF* sample and (e–h) the *PZNF* sample.

The two samples were further characterized by HRTEM and XRD to reveal their crystal structures. As shown in Figs. 2d and h, the HRTEM images of both samples reveal parallel crystal planes with a measured spacing of ~0.24 nm characteristic of the (101) plane of ZnO. The XRD patterns of both samples (Fig. 3a) show diffraction peaks that can be indexed to the (100), (002), (101), (102), (110), (103), (200), (112), (201), (004), (202) and (104) planes of the ZnO wurtzite

crystal structure (JCPDS 89-0510), and no diffraction peaks related to any impurity phases. These

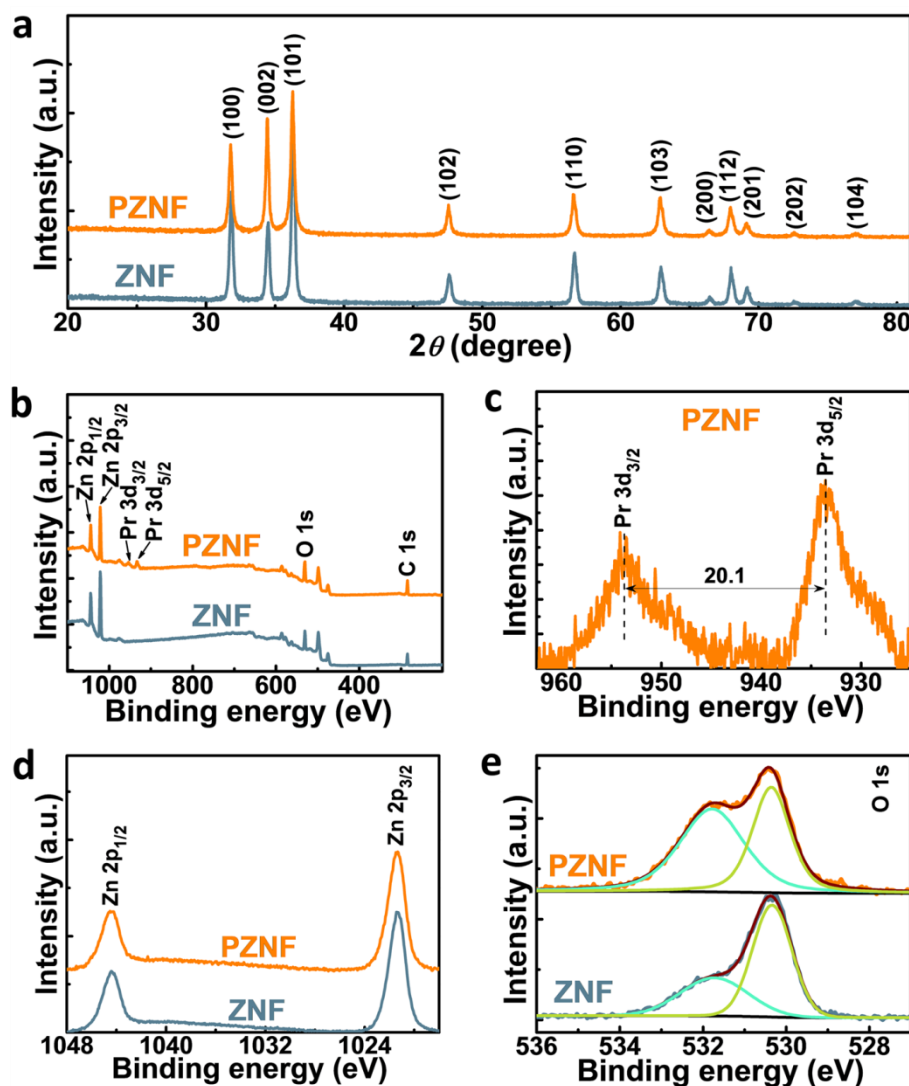HRTEM and XRD data confirm the crystalline quality of the ZnO in both nanofiber samples.

Fig. 3. (a) XRD patterns and (b) XPS survey spectra of the *ZNF* and *PZNF* samples. (c) High-resolution XPS

spectrum of the Pr 3d region for the *PZNF* sample. High-resolution XPS spectra of (d) the Zn 2p region and the O

1s region for the *ZNF* and *PZNF* samples.

XPS was used to explore the chemical compositions of the nanofiber samples. Survey spectra

of the *ZNF* and *PZNF* samples are shown in Fig. 3b. In addition to the Zn and O peaks, the *PZNF*

sample shows two peaks that confirm the presence of Pr. XPS is a surface sensitive technique, so

the finding that the measured Pr/Zn atomic ratio (0.11:1.00) is much larger than that in the

precursor mixture (0.01:1.00) implies that a large fraction of the Pr is at the surface of (or at the

interface between) the ZnO nanocrystallites. The O/Zn atomic ratios derived from the XPS data

for the *PZNF* and *ZNF* samples are, respectively, 1.57:1.00 and 1:03:1.00 − indicating that the *PZNF* sample supports relatively more oxygen containing species on its surface.

The high-resolution Pr 3d XPS spectrum (Fig. 3c) reveals Pr $3d_{3/2}$ and Pr $3d_{5/2}$ peaks at, respectively, 953.7 eV and 933.6 eV with an energy separation of 20.1 eV, implying that the Pr in the *PZNF* sample is present as Pr^{3+} or Pr^{4+} [43]. The high-resolution Zn 2p spectra of the two samples (Fig. 3d) are quite similar, but the profiles of the high-resolution O 1s spectra of the *PZNF* and *ZNF* samples (Fig. 3e) are clearly different. Both O 1s spectra can be deconvolved into two sub-peaks. The peak centered at 530.3 eV is a signature of the O^{2-} ion in the ZnO wurtzite structure, while the 531.8 eV peak is attributable to adsorbed oxygen species on the surface and/or oxygen ions in oxygen-deficient regions [44−46]. The different sub-peak ratios in the O 1s spectra reinforce the findings from the XPS data that the *PZNF* sample supports relatively more surface adsorbed oxygen species than the *ZNF* sample.

PL spectra of the *ZNF* and *PZNF* samples measured in air at temperatures ranging from room temperature (RT) to $T = 210$ °C are presented in Figs. 4a and b, respectively. The RT PL spectrum of the *ZNF* sample consists of a sharp near-band-edge UV emission centered at 382 nm and a broad, defect-related, visible-band emission. The latter can be further partitioned into an oxygen-deficiency-related green emission centered at 520 nm [47] and an oxygen-rich-related orange emission centered at 600 nm [48]. With increasing temperature, both the UV and visible-band emissions from the *ZNF* sample shift to longer wavelengths and decline in intensity − observations that match previous findings [18] and are not considered further. The PL spectra of the *PZNF* sample show similar profiles and temperature-dependences to those of the *ZNF* sample, but also two clear differences: (1) The ratio of the peak intensities of the visible band and UV emissions ($I_{visible}/I_{UV}$) from the *PZNF* sample at any given temperature is much smaller than that from the *ZNF* sample, implying that the ZnO in the *PZNF* sample has a higher crystalline quality and thus a higher UV emission efficiency; (2) The visible band emission of the *PZNF* sample is dominated by an oxygen-deficiency-related component, the relative importance of which falls as T is increased, *e.g.* $I_{visible}/I_{UV}$ declines from 0.98 at RT to 0.20 at $T = 115$ °C. The *ZNF* sample, in contrast, shows a relatively strong oxygen-rich-related emission which decreases more slowly than the oxygen-deficiency-related emission with increasing temperature and dominates the visible band emission at $T \geq 80$ °C. The $I_{visible}/I_{UV}$ ratio for the *ZNF* sample declines from 2.19 at RT to
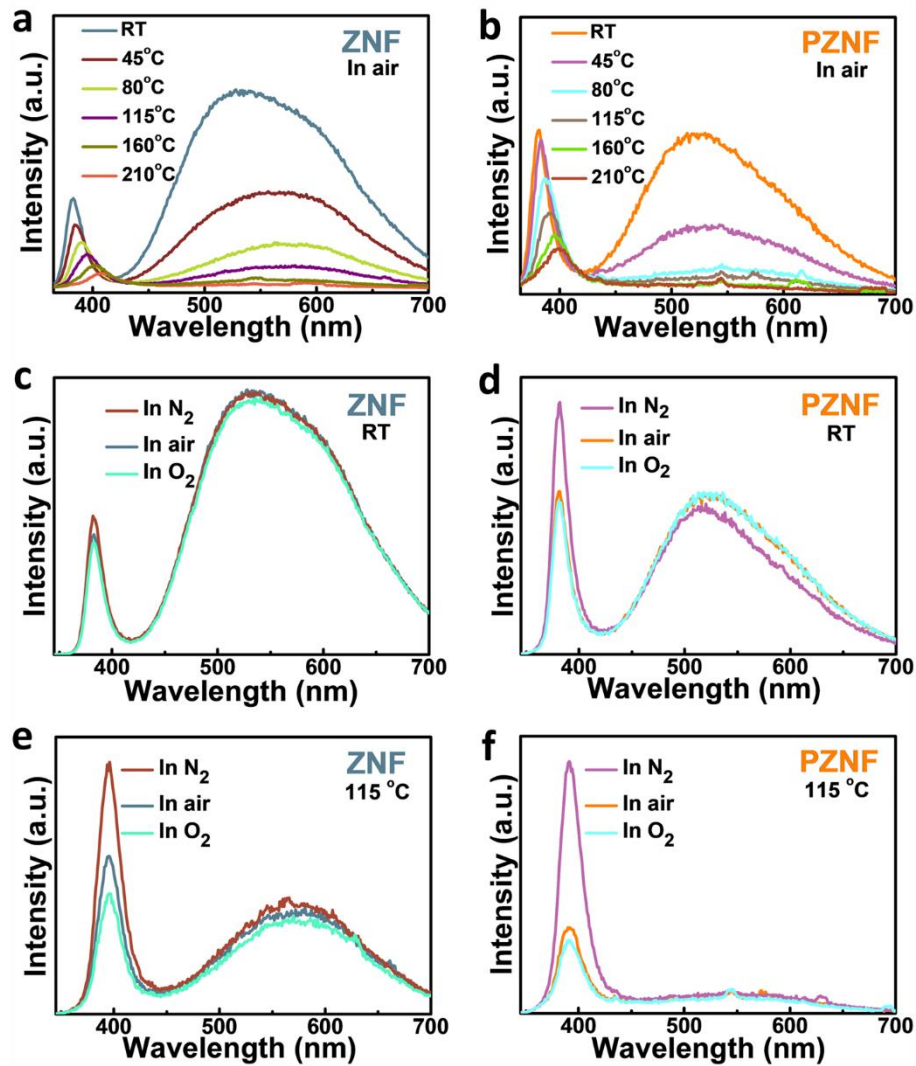
0.65 at T = 115 °C.

Fig. 4. (a–b) Temperature-dependent PL spectra, (c–d) PL spectra measured in nitrogen, air and oxygen atmospheres at RT, and (e–f) PL spectra measured in nitrogen, air and oxygen atmospheres at T = 115 °C of the *ZNF* and *PZNF* samples.

A sample temperature of 115 °C is too low to cause any substantial reduction of defects in the inner (bulk) part of the crystallites but could have a substantial influence on surface defects related to the physical and chemical adsorption of gaseous species. Thus, it is rational to conclude that the ZnO in the *ZNF* sample has relatively poorer crystalline quality with some oxygen-rich-related defects located inside the crystallites, while the ZnO in the *PZNF* sample has higher crystalline quality and contains a higher density of oxygen-deficiency-related defects at the crystallite

8

surfaces and interfaces – which are beneficial to the adsorption of oxygen species and thus improve the sensing performance of such gas sensors [49]. The T-dependent PL properties of the *PZNF* sample can be understood if the surfaces and interfaces of the ZnO nanocrystallites are Pr-rich, and the smaller average crystallite size facilitates higher crystalline quality via the calcination process.

The oxygen gas sensing properties of the *ZNF* and *PZNF* samples were evaluated by measuring their PL in nitrogen, air and oxygen atmospheres, respectively. The RT PL measurements show that the peak intensity of the UV emission, I_{UV}, from the *ZNF* and the *PZNF* samples both decrease as the O_2 concentration is increased (Figs. 4c and d). Compared to $R = 19\%$ for the *ZNF* sample, the *PZNF* sample presents a much higher RT sensing response, $R = 39\%$. This exceeds the value ($R = 30.7\%$) reported for O_2 sensing at $T = 150 \, °C$ with ZnO nanorods grown by pulsed laser deposition [18]. Even more promisingly, sensing responses of $R = 52\%$ and 71% were obtained with the *ZNF* and *PZNF* samples when measuring the PL at $T = 115 \, °C$. The latter value surpasses most reported optical oxygen sensing responses using ZnO nanomaterials [18,26].

Temperature has been suggested to have a key influence on the gas sensing performance of many oxides. Fig. 5a shows the T-dependence of R for both the *ZN*F and *PZNF* samples over the temperature range from RT to $T = 208 \, °C$. For both samples, R increases steeply up to $T \sim 115 \, °C$ but thereafter increases only slowly. This behavior is likely to be attributable to adsorbed water-related species. Since I_{UV} decreases with increasing T (Figs. 4a and b) and small I_{UV} values are not conducive to good signal detection or R determination, $115 \, °C$ was selected as the optimal working temperature.

The dynamic I_{UV} response of the *PZNF* sample to oxygen at $T = 115 \, °C$ was investigated by changing the partial pressure of O_2 in an N_2/O_2 mixture maintained at a total pressure $p = 1$ bar. As Fig. 5b shows, I_{UV} decreased with increasing oxygen concentration and yielded a clearly measurable response even at low (*e.g.* 3%) oxygen concentrations. The measured response and recovery times of the *PZNF* sample are of the order of 2 and 8 min, respectively, which are both some 5 min shorter than the corresponding response and recovery times of the *ZNF* sample. The dynamic I_{UV} of the *PZNF* sample in 0% O_2 (*i.e.* 100% N_2) and in 100% O_2 at $T = 115 \, °C$ and $p = 1$ bar is shown in Fig. 5c. These data confirm the good recoverability and reproducibility of the oxygen sensing and illustrate the promise of the *PZNF* sample as an optical oxygen sensor.
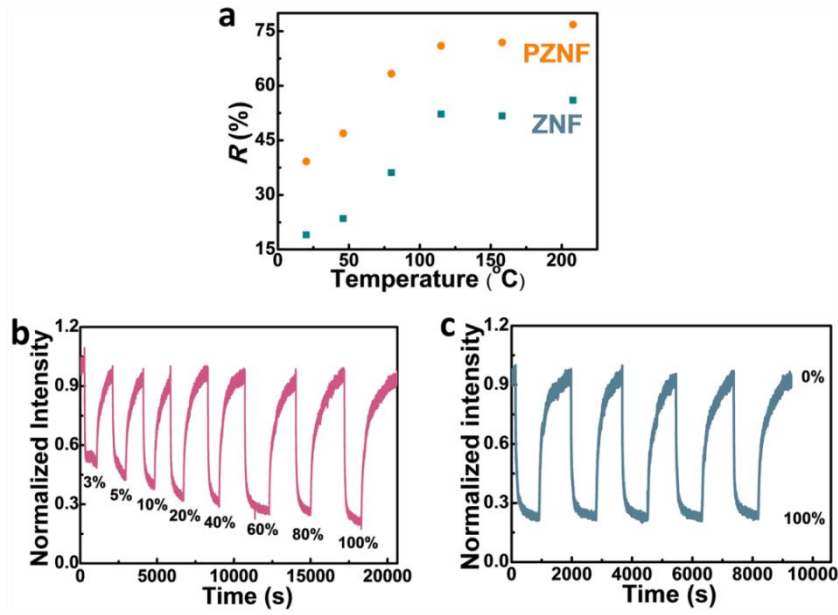
Fig. 5. (a) Temperature-dependent R of the *ZNF* and *PZNF* samples. (b) Dynamic UV emission intensity of the *PZNF* sample to different concentrations of O_2 (in N_2) at T = 115 °C and p = 1 bar. (c) Dynamic UV emission intensity of the *PZNF* sample in 0% O_2 (100% N_2) and in 100% O_2.

It is well known that adsorption/desorption of oxygen species on a ZnO surface can trap or release electrons, causing an expansion or contraction of the electron depletion layer at the surface (Fig. 1) [18,19]. Since the depletion layer makes little or no contribution to the UV emission [19], I_{UV} is mainly dependent on the volume of the "non-depleted" region beneath the depletion layer. Thus the response of an I_{UV}-based oxygen sensor is very dependent on the surface conditions (*e.g.* the surface area to volume (S/V) ratio and the number and nature of the active sites for oxygen adsorption) of the ZnO material. Based on the above sensing mechanisms, likely reasons for the superior oxygen sensing performance of the *PZNF* sample (*cf.* the *ZNF* sample) include: (1) The *PZNF* sample has a much larger S/V ratio (as shown in Fig. 2); and (2), as noted previously, Pr introduces additional active sites on the sample surface that facilitate oxygen adsorption [28−31]. Further, the PL data indicates that the *PZNF* sample has higher crystalline quality (*i.e.* less defect-related visible emission from the inner part of the sample, Fig. 4) and thus a higher UV emission efficiency. This is important: high intrinsic emission efficiencies and emission intensities are critical for high-performance I_{UV}-based gas sensing, since the sensing relies on the accurate measurement of reductions in emission intensity.

4. Conclusions

Pure and Pr-modified ZnO nanofibers have been synthesized using a common electrospinning-calcination technique. Compared with the pure ZnO nanofibers – which are found to contain many compact nanocrystallites – the Pr-modified ZnO nanofibers have larger diameter and present more porous structures incorporating many smaller nanocrystallites of higher crystalline quality. Pr preferentially locates at the surface of the nanocrystallites and facilitates further adsorption of oxygen species. As a result, the Pr-modified ZnO nanofibers exhibit a higher UV emission efficiency and a much-enhanced UV emission-based O_2 sensing performance relative to that of the pure ZnO nanofibers. O_2 sensing responses $R = 39\%$ and 71% have been demonstrated at room temperature and at $T = 115$ °C, respectively – values that exceed most optical oxygen sensing performances of ZnO nanomaterials reported hitherto. The present study illustrates the considerable promise of electrospun Pr-modified ZnO nanofibers for optical gas sensing applications.

References

[1] B. Yao, C. Yu, Y. Wu, S.-W. Huang, H. Wu, Y. Gong, Y. Chen, Y. Li, C.W. Wong, X. Fan, Y. Rao, Graphene-enhanced Brillouin optomechanical microresonator for ultrasensitive gas detection, Nano Lett. 17 (2017) 4996−5002.

[2] Y. Zhang, L.-T. Lim, Colorimetric array indicator for NH_3 and CO_2 detection, Sens. Actuators B 255 (2018) 3216−3226.

[3] C. Boelsma, L.J. Bannenberg, M.J. van Setten, N.-J. Steinke, A.A. van Well, B. Dam, Hafnium – an optical hydrogen sensor spanning six orders in pressure, Nat. Commun. 8 (2017) 15718.

[4] B.N. Shivananju, W. Yu, Y. Liu, Y. Zhang, B. Lin, S. Li, Q. Bao, The roadmap of graphene-based optical biochemical sensors, Adv. Funct. Mater. 27 (2017) 1603918.

[5] I.B. Tahirbegi, J. Ehgartner, P. Sulzer, S. Zieger, A. Kasjanow, M. Paradiso, M. Strobl, D. Bouwes, T. Mayr, Fast pesticide detection inside microfluidic device with integrated optical pH, oxygen sensors and algal fluorescence, Biosens. Bioelectron. 88 (2017) 188–195.

[6] C. Jiang, N. Zhong, C. Luo, H. Lin, Y. Zhang, H. Peng, C.-G. Duan, (Diisopropylammonium)$_2$MnBr$_4$: a multifunctional ferroelectric with efficient green-emission and excellent gas sensing properties, Chem. Commun. 53 (2017) 5954–5957.

[7] M. Eltermann, V. Kiisk, A. Berholts, L. Dolgov1, S. Lange, K. Utt, R. Jaaniso, Modeling of luminescence-based oxygen sensing by redox-switched energy transfer in nanocrystalline TiO$_2$:Sm^{3+}, Sens. Actuators B 265 (2018) 556–564.

[8] W. Tang, Y. Sun, S. Wang, B. Du, Y. Yin, X. Liu, B. Yang, W. Cao, M. Yu, Pr^{3+}-Doped (K$_{0.5}$Na$_{0.5}$)NbO$_3$ as high response optical oxygen sensing agent, J. Mater. Chem. C 4 (2016) 11508–11513.

[9] L. Zhu, W. Zeng, Room-temperature gas sensing of ZnO-based gas sensor: A review, Sens. Actuators A 267 (2017) 242–261.

[10] Y. Li, S. Wang, P. Hao, J. Tian, H. Cui, X. Wang, Soft-templated formation of double-shelled ZnO hollow microspheres for acetone gas sensing at low concentration/near room temperature, Sens. Actuators B 273 (2018) 751–759.

[11] X. Liu, Y. Sun, M. Yu, Y. Yin, B. Du, W. Tang, T. Jiang, B. Yang, W. Cao, M.N.R. Ashfold, Enhanced ethanol sensing properties of ultrathin ZnO nanosheets decorated with CuO nanoparticles, Sens. Actuators B 255 (2018) 3384–3390.

[12] M. Kaur, S. Kailasaganapathi, N. Ramgir, N. Datta, S. Kumar, A,K, Debnath, D.K. Aswal, S.K. Gupta, Gas dependent sensing mechanism in ZnO nanobelt sensor, Appl. Surf. Sci. 394 (2017) 258–266.

[13] R.S. Ganesh, G.K. Mani, R. Elayaraja, E. Durgadevi, M. Navaneethan, S. Ponnusamy, K. Tsuchiya, C. Muthamizhchelvan, Y. Hayakawa, ZnO hierarchical 3D-flower like architectures and their gas sensing properties at room temperature, Appl. Surf. Sci. 449 (2018) 314–321.

[14] M. Li, E.G. Seebauer, Coverage-dependent adsorption thermodynamics of oxygen on ZnO(0001), Appl. Surf. Sci. 397 (2017) 220–225.

[15] J.-H. Lim, C.-K. Kang, K.-K. Kim, I.-K. Park, D.-K. Hwang, S.-J. Park, UV

electroluminescence emission from ZnO light-emitting diodes grown by high-temperature radiofrequency sputtering, Adv. Mater. 18 (2006) 2720–2724.

[16] Y. Yin, Y. Sun, M. Yu, X. Liu, B. Yang, D. Liu, S. Liu, W. Cao, M.N.R. Ashfold, Reagent concentration dependent variations in the stability and photoluminescence of silica-coated ZnO nanorods, Inorg. Chem. Front. 2 (2015) 28–34.

[17] S.T. Tan, C.H. Tan, W.Y. Chong, C.Y. Chi, A.A. Umar, R.T. Ginting, H.B. Lee, K.S. Lim, M. Y, M.M. Salleh, Microwave-assisted hydrolysis preparation of highly crystalline ZnO nanorod array for room temperature photoluminescence-based CO gas sensor, Sens. Actuators B 227 (2016) 304–312.

[18] X. Liu, Y. Sun, M. Yu, Y. Yin, B. Yang, W. Cao, M.N.R. Ashfold, Incident fluence dependent morphologies, photoluminescence and optical oxygen sensing properties of ZnO nanorods grown by pulsed laser deposition, J. Mater. Chem. C 3 (2015) 2557–2562.

[19] X. Liu, B. Du, Y. Sun, M. Yu, Y. Yin, W. Tang, C. Chen, L. Sun, B. Yang, W. Cao, M.N.R. Ashfold, Sensitive room temperature photoluminescence-based sensing of H_2S with novel CuO-ZnO nanorods, ACS Appl. Mater. Interfaces 8 (2016) 16379–16385.

[20] D. Valerini, A. Cretì, A.P. Caricato, M. Lomascolo, R. Rella, M. Martino, Optical gas sensing through nanostructured ZnO films with different morphologies, Sens. Actuators B 145 (2010) 167–173.

[21] M. Madel, J. Jakob, F. Huber, B. Neuschl, S. Bauer, Y. Xie, I. Tischer, K. Thonke, Optical gas sensing by micro-photoluminescence on multiple and single ZnO nanowires, Phys. Status Solidi 212 (2015) 1810–1816.

[22] F. Cao, C. Li, M. Li, H. Li, X. Huang, B. Yang, Direct growth of Al-doped ZnO ultrathin nanosheets on electrode for ethanol gas sensor application, Appl. Surf. Sci. 447 (2018) 173–181.

[23] K. Yadav, S.K. Gahlaut, B.R. Mehta, J.P. Singh, Photoluminescence based H_2 and O_2 gas sensing by ZnO nanowires, Appl. Phys. Lett. 108 (2016) 071602.

[24] Cretì, D. Valerini, A. Taurino, F. Quaranta, M. Lomascolo, R. Rella, Photoluminescence quenching processes by NO_2 adsorption in ZnO nanostructured films, J. Appl. Phys. 111 (2012) 073520.

[25] R. Aad, V. Simic, C.L. Le, L. Rocha, V. Sallet, C. Sartel, A. Lusson, C. Couteaua, G.

Lerondel, ZnO nanowires as effective luminescent sensing materials for nitroaromatic derivatives, Nanoscale 5 (2013) 9176−9180.

[26] J.R. Sanchez-Valencia, M. Alcaire, P. Romero-Gómez, M. Macias-Montero, F.J. Aparicio, A. Borras, A.R. Gonzalez-Elipe, A. Barranco, Oxygen optical sensing in gas and liquids with nanostructured ZnO thin films based on exciton emission detection, J. Phys. Chem. C 118 (2014) 9852−9859.

[27] C. Wang, S. Ma, A. Sun, R. Qin, F. Yang, X. Li, F. Li, X. Yang, Characterization of electrospun Pr-doped ZnO nanostructure for acetic acid sensor, Sens. Actuators B 193 (2014) 326−333.

[28] C. Su, Y. Li, S. Li, L. Liu, X. Guo, H. Lian, X. Guan, Excellent ethanol sensing properties of Pr-doped α-Fe$_2$O$_3$ nanotubes, J. Mater. Sci.: Mater. Electron. 27 (2016) 6829−6834.

[29] X.L. Xu, Y. Chen, G.H. Zhang, S.H. Yan, H.Q. Bian, Q. Chen, Y. Lu, S.Y. Ma, Fabrication of Pr-doped SnO$_2$, spherical core-shell nanostructure with wrinkly shell and the gas sensing properties, Mater. Lett. 195 (2017) 159−163.

[30] Q. Ge, S.Y. Ma, Y.B. Xu, X.L. Xu, H. Chen, Z. Qiang, H.M. Yang, L. Ma, Q.Z. Zeng, Preparation, characterization and gas sensing properties of Pr-doped ZnO/SnO$_2$ nanoflowers, Mater. Lett. 191 (2017) 5−9.

[31] Q. Chen, S.Y. Ma, H.Y. Jiao, B.Q. Wang, G.H. Zhang, D.J. Gengzang, L.W. Liu, H.M. Yang, Sodium alginate assisted hydrothermal method to prepare praseodymium and cerium co-doped ZnSn(OH)$_6$ hollow microspheres and synergistically enhanced ethanol sensing performance, Sens. Actuators B 252 (2017) 295−305.

[32] I. Dascalu, D. Culita, J.M. Calderon-Moreno, P. Osiceanu, C. Hornoiu, M. Anastasescu, S. Somacescu, M. Gartner, Structural, textural, surface chemistry and sensing properties of mesoporous Pr, Zn modified SnO$_2$–TiO$_2$ powder composites, Ceram. Int. 42 (2016) 14992–14998.

[33] Y. Wang, Z. Wei, P. Li, G. Li, K. Lian, W. Zhang, S. Zhuiykov, J. Hu, Pr$_6$O$_{11}$-functionalized SnO$_2$ flower-like architectures for highly efficient, stable, and selective acetone detection, IEEE Sen. J. 18 (2018) 933–940.

[34] P. Ilanchezhiyan, G.M. Kumar, M. Subramanian, R. Jayavel, Effect of Pr doping on the structural and optical properties of ZnO nanorods, Mater. Sci. Eng. B 175 (2010) 238−242.

[35] R.S. Sreedharan, R. Vinodkumar, I. Navas, R. Prabhu, V.P.M. Pillai, Influence of Pr doping on the structural, morphological, optical, luminescent and non-linear optical properties of RF-sputtered ZnO films, JOM 68 (2015) 341−350.

[36] M.-H Wang, Z.-Y Zhao, T.-T Liu, Synthesis of Pr-doped ZnO nanoparticles by sol-gel method and varistor properties study, J. Alloys Compd. 621 (2015) 220−224.

[37] Y. Meng, G. Liu, A. Liu, Z. Guo, W. Sun, F. Shan, Photochemical activation of electrospun In_2O_3 nanofibers for high-performance electronic devices, ACS Appl. Mater. Interfaces 9 (2017) 10805−10812.

[38] Y.-Y. Cho, C. Kuo, Optical and electrical characterization of electrospun Al-doped zinc oxide nanofibers as transparent electrodes, J. Mater. Chem. C 4 (2016) 7649−7657.

[39] S. Bai, S. Chen, Y. Zhao, T. Guo, R. Luo, D. Li, A. Chen, Gas sensing properties of Cd-doped ZnO nanofibers synthesized by the electrospinning method, J. Mater. Chem. A 2 (2014) 16697−16706.

[40] F. Pantò, S.G. Leonardi, E. Fazio, P. Frontera, A. Bonavita, G. Neri, P. Antonucci, F. Neri, S. Santangelo, CO_2 sensing properties of electro-spun Ca-doped ZnO fibres, Nanotechnology 29 (2018) 305501.

[41] P. Jaroenapibal, P. Boonma, N. Saksilaporn, M. Horprathum, V. Amornkitbamrung, N. Triroj, Improved NO_2 sensing performance of electrospun WO_3 nanofibers with silver doping, Sens. Actuators B 255 (2018) 1831−1840.

[42] A. Khalil, J.J. Kim, H.L. Tuller, G.C. Rutledge, R. Hashaikeh, Gas sensing behavior of electrospun nickel oxide nanofibers: Effect of morphology and microstructure, Sens. Actuators B 227 (2016) 54−64.

[43] F.H Aragón, I. Gonzalez, J.A.H. Coaquira, P. Hidalgo, H.F. Brito, J.D. Ardisson, W.A.A. Macedo, P.C. Morais, Structural and surface study of praseodymium-doped SnO_2 nanoparticles prepared by the polymeric precursor method, J. Phys. Chem. C 119 (2015) 8711−8717.

[44] K.H. Tam, C.K. Cheung, Y.H. Leung, A.B. Djurisic, C.C. Ling, C.D. Beling, S. Fung, W.M. Kwok, W.K. Chan, D.L. Phillips, L. Ding, W.K. Ge, Defects in ZnO nanorods prepared by a hydrothermal method, J. Phys. Chem. B 110 (2006) 20865−20871.

[45] M. Baek, D. Kim, K. Yong, Simple but effective way to enhance photoelectrochemical

solar-water-splitting performance of ZnO nanorod arrays: Charge-trapping $Zn(OH)_2$ annihilation and oxygen vacancy generation by vacuum annealing, ACS Appl. Mater. Interfaces 9 (2017) 2317−2325.

[46] S. Brahma, C.-W. Yang, C.-H. Wu, F.-M. Chang, T.-J. Wu, C.-S. Huang, K.-Y. Lo, The optical response of ZnO nanorods induced by oxygen chemisorption and desorption, Sens. Actuators B 259 (2018) 900-907.

[47] R. Yousefi, Effects of Sn atoms on formation of ZnO nanorings, CrystEngComm, 17 (2015) 2698–2704.

[48] Y. Yin, Y. Sun, M. Yu, X. Liu, B. Yang, D. Liu, S. Liu, W. Cao, M.N.R. Ashfold, Arrays of nanorods composed of ZnO nanodots exhibiting enhanced UV emission and stability, Nanoscale 6 (2014) 10746-10751.

[49] V. Khorramshahi, J. Karamdel, R. Yousefi, High acetic acid sensing performance of Mg-doped ZnO/rGO nanocomposites, Ceram. Int. 45 (2019) 7034–7043.